Journal of Materials Chemistry A

ROYAL SOCIETY OF CHEMISTRY

PAPER

View Article Online
View Journal | View Issue

Cite this: J. Mater. Chem. A, 2022, 10, 24056

Co, Fe and N co-doped 1D assembly of hollow carbon nanoboxes for high-performance supercapacitors†

Minjun Kim,[a] Chaohai Wang, *[b] Jacob Earnshaw,[a] Teahoon Park, [c] Nasim Amirilian, [a] Aditya Ashok, [a] Jongbeom Na, [d] Minsu Han,[a] Alan E. Rowan,[a] Jiansheng Li, [e] Jin Woo Yi*[c] and Yusuke Yamauchi *[a]

Received 2nd September 2022
Accepted 17th October 2022

DOI: 10.1039/d2ta06950d

rsc.li/materials-a

In this study, we successfully demonstrate the synthesis of a novel necklace-like Co, Fe, and N co-doped one-dimensional (1D)-assembly of hollow carbon nanoboxes (1D-HCNB-*x*) and its potential for a supercapacitor application. The unique hybrid nanoarchitecture of 1D-HCNB-*x* consisting of hollow zero-dimensional (0D) carbons arrayed along the 1D carbon nanofiber is highly desirable for supercapacitors because it presents improved rate capability and high axial electron conductivity. The presence of Fe, Co and N dopants in the carbon matrix also generates pseudocapacitance to further improve specific capacitance. The optimized 1D-HCNB-900 generates a specific capacitance of 370.0 F g^{-1} at a current density of 2 A g^{-1}, high rate capability and tolerance, and great cyclability.

Introduction

With growing concerns on environment and sustainability, more efficient energy storage devices are highly demanded in the current energy cycle.[1–3] Among different types of energy storage devices, high-performance supercapacitors are of great interest because of their unique advantages, including high power density, outstanding cyclability, long life, and short charging time, that are often not achieved in secondary batteries.[1] There are two types of energy storage mechanisms of supercapacitors, namely, electrical double-layer capacitance (EDLC) and pseudocapacitance.[4] The EDLC is known to be heavily influenced by specific surface area and porosity of electrode materials because it occurs on the surface in the form of an electrical double-layer.[2,4] Among various types of electrode materials, porous carbon materials typically exhibit great EDLC-based energy storing behavior.[5] In addition, the porous carbon materials can be doped or hybridized with redox-active atoms or molecules to generate pseudocapacitance.[4,6] Therefore, it is highly desirable to design and synthesize porous carbon materials with high specific surface area, tuned porosity, and abundant redox-active sites to facilitate both EDLC and pseudocapacitance to achieve high-performance supercapacitors.[7,8]

While aiming for a high specific surface area with abundant heteroatom doping, the unique nanoarchitecture of porous carbon materials should be carefully considered to maximize the electrochemically accessible/active portion of the specific surface area.[9,10] For example, hollow carbon materials are known to promote ionic diffusion as their hollow cavities serve as reservoirs of electrolyte ions, hence shortening the required diffusion distance of ions.[11,12] Consequently, hollow carbon materials generally demonstrate high rate capabilities in energy storage applications. In addition, carbon materials with one-dimensionality (1D), such as carbon nanotubes, graphene fibers, carbon nanofibers, and carbon nanorods, are highly beneficial as electrode materials because they exhibit high mass and charge transfer along the longitudinal axis consisting of an extensive network of sp^2/sp^3-hybridized carbons.[13–15] Despite high electrical conductivity, 1D carbon materials often face side-by-side agglomeration/aggregation, hence greatly limiting the electrochemical usage of their surface areas.[4,16,17]

Herein, we present a novel necklace-like 1D assembly of hollow carbon nanoboxes (1D-HCNB-*x*) which successfully integrates the advantage of hollow carbon materials and 1D carbon materials to overcome morphological limitations and achieve high specific capacitance as supercapacitor electrode

[a]Australian Institute for Bioengineering and Nanotechnology (AIBN) and School of Chemical Engineering, The University of Queensland, Brisbane, Queensland 4072, Australia. E-mail: y.yamauchi@uq.edu.au

[b]Henan Key Laboratory of Water Pollution Control and Rehabilitation Technology, School of Municipal and Environmental Engineering, Henan University of Urban Construction, Pingdingshan 467036, People's Republic of China . E-mail: chaohai@hncj.edu.cn

[c]Carbon Composite Department, Composites Research Division, Korea Institute of Materials Science (KIMS), Changwon-si 51508, Gyeongsangnam-do, Republic of Korea. E-mail: yjw0628@kims.re.kr

[d]Materials Architecturing Research Center, Korea Institute of Science and Technology (KIST), 5 Hwarang-ro 14-gil, Seongbuk-gu, Seoul 02792, Republic of Korea

[e]Key Laboratory of Jiangsu Province for Chemical Pollution Control and Resources Reuse, School of Environment and Biological Engineering, Nanjing University of Science and Technology, Nanjing, 210094, China

† Electronic supplementary information (ESI) available. See DOI: https://doi.org/10.1039/d2ta06950d

materials. To prepare 1D-HCNB-*x*, Co and Fe-based Prussian blue analogue (CoFe-PBA) particles were first electrospun with polyacrylonitrile (PAN) to form PAN nanofibers embedding the CoFe-PBA particles (1D-CoFe-PBA), hence forming a necklace-like nanoarchitecture.[18] The 1D-CoFe-PBA was then subjected to an initial carbonization, acid leaching, and then a second carbonization at *x* °C to finally obtain 1D-HCNB-*x*. The 1D-HCNB-*x* is highly suitable for supercapacitors due to the following properties. (1) As the 1D-CoFe-PBA serves as a carbon precursor, it successfully incorporates abundant redox-active Co, Fe, and N heteroatoms into the carbon matrix to increase capacitance *via* pseudocapacitance.[7,19,20] (2) The presence of Co/Fe during carbonization enhances the graphitization of carbon atoms *via* thermal catalytic activity. The increased level of graphitization, in turn, leads to greater electrical conductivity.[21,22] (3) Its 1D nature increases the exposure of surface area and enhances both mass and charge transfer along the axial structure.[13] (4) The presence of clear hollowness ensures the efficient diffusion of electrolytes throughout the electrochemically accessible surface area even at high current densities or scan rates.[11,12] (5) The presence of hollow junctions in the 1D morphology prevents the loss of specific surface area by severe aggregation. The optimized 1D-HCNB-900, therefore, demonstrates a superior specific capacitance of 398.5 F g^{-1} at 1 mV s^{-1} (370.0 F g^{-1} at 2 A g^{-1}) in 2 M KOH electrolyte, and an outstanding electrochemical stability with no notable decay of specific capacitance over 15 000 cycles.

Experimental methods

Materials and reagents

Potassium hexacyanocobaltate(III) ($K_3[Co(CN)_6]$), and polyvinyl pyrrolidone (PVP, K30) were purchased from Sinopharm Chemical Reagent Co., Ltd (Shanghai, China). Ferrous sulfate heptahydrate ($FeSO_4 \cdot 7H_2O$), *N*,*N*-dimethylformamide (DMF), polyacrylonitrile (PAN, MW = 150 000), and other organic solvents were purchased from Sigma-Aldrich.

Synthesis of CoFe-PBA nanoparticles

6.0 g PVP was dissolved in 200 mL of deionized water (DIW) with continuous stirring. After complete dissolution of PVP, 1.8 mL HCl was added in a drop-wise manner and stirred for 10 minutes. Next, 0.332 g $K_4[Co(CN)_6] \cdot 3H_2O$ was added to the mixture and stirred for another 1 hour at room temperature. A peristaltic pump was used to add 200 mL of 2.1 mg mL^{-1} $FeSO_4 \cdot 7H_2O$ in the above solution with a flow rate of 4 mL min^{-1}. The Co–Fe PBA was obtained after stirring for 24 hours at room temperature. The products were collected by centrifugation and washed 3 times with DIW and anhydrous ethanol, and finally dried at 60 °C.

Synthesis of 1D-CoFe-PBA

1D-CoFe-PBA was prepared according to the previous literature.[18] 1.3 g CoFe-PBA nanoparticles were added to 5.0 mL DMF with sonication until it was well dispersed. Then, 0.65 g PAN was added to the solution with stirring at 60 °C for 4 hours to obtain the electrospinning precursor. The electrospinning process was carried out at an injection speed of 0.15 mm min^{-1} by applying a high positive voltage (10 kV) with a collecting distance of 15 cm.

Synthesis of 1D-CoFe-PBA-derived carbon (1D-CoFe-PBA/C)

The above obtained 1D-CoFe-PBA were placed in a tube furnace and then heated to 800 °C for 4 hours at a heating rate of 5 °C min^{-1} in an N_2 atmosphere.

Synthesis of 1D-HCNB-*x*

To prepare 1D-HCNB-*x*, 1D-CoFe-PBA/C was stirred at 500 rpm in 3 M H_2SO_4 at 100 °C for 24 hours. After acid washing, the sample was thoroughly washed with DIW until neutral pH was achieved, and dried at 60 °C. After drying, the sample was subjected to direct carbonization at a certain temperature (800 or 900 or 1000 °C) at a heating rate of 5 °C min^{-1} to obtain 1D-HCNB-*x* (where *x* represents the carbonization temperature).

Material characterization

Transmission electron microscope (TEM) images were obtained by using an HT7700 (Hitachi) at 120 kV, and field-emission scanning electron microscope (FESEM) images were obtained by using a Quanta 250 FEG (FEI) at 5.0 kV. Scanning transmission electron microscope (STEM) and high-resolution TEM (HRTEM) images were obtained by using an HF5000 (Hitachi) at 200 kV. Powder X-ray diffraction (PXRD, D8 Advance, Bruker) was used to study the crystal structures of materials with Cu-Kα radiation at 40 kV and 40 mA. The elemental composition and the electronic structure were investigated by X-ray photoelectron spectroscopy (XPS) using mono-Al Kα (1486.6 eV) X-rays. Nitrogen adsorption and desorption isotherms were measured by using a BELSORP Max II surface area and pore size analyzer at liquid nitrogen temperature (77 K). Pore size distributions were obtained by the non-local density functional theory (NLDFT) model.

Electrochemical measurement

The electrochemical measurements were carried out using a CHI660E (CH Instruments) in a typical three-electrode system. A Pt wire (23 cm) and Hg/HgO electrode saturated with 1 M NaOH were used as the counter electrode and the reference electrode, respectively. Electrode ink was prepared by sonicating active material (10 mg), poly(vinylidene fluoride) (PVDF, 1.25 mg), and carbon black (1.25 mg) in a 8 : 1 : 1 weight ratio in 1 mL *N*-methyl-2-pyrrolidone (NMP) solution. A volume of 100 μL of the electrode ink was drop-cast on a 1 cm × 1 cm graphite plate connected with copper wire. The electrode ink was dried at 50 °C in an air-forced oven. The electrochemical measurement was conducted in a 2 M KOH electrolyte solution. Cyclic voltammetry (CV) and galvanostatic charge–discharge (GCD) were conducted at various scan rates and current densities, respectively. Electrochemical impedance spectroscopy (EIS) was performed at the open circuit potential with an amplitude of 10 mV

between 100 kHz and 10 mHz. The cyclability test was conducted with 15 000 consecutive cycles of GCD at 10 A g^{-1}.

The specific capacitance (C_{sp}, F g^{-1}) was calculated from the CV curves by using the following equation:

$$C_{sp} = \frac{1}{2 \times v \times \Delta V \times m} \int I dV$$

where v is the scan rate (mV s^{-1}), ΔV is the potential window (V), $\int I dV$ is the integrated area of the CV curve, and m is the mass of the active material (g).

The C_{sp} (F g^{-1}) was calculated from the GCD curves by using the following equation:

$$C_{sp} = \frac{I \times \Delta t}{\Delta V \times m}$$

where I is the current applied (A), Δt is discharge time, ΔV is the potential window (V) of the GCD curve, and m is the mass of the active material (g).

The coulombic efficiency (η) was calculated from the GCD curves by using the following equation:

$$\eta = \frac{t_D}{t_C} \times 100\%$$

where t_D is the discharge time (s) and t_C is the charge time (s).

The imaginary part of complex capacitance, $C(\omega)$, was derived from the following equations:

$$C(\omega) = C'(\omega) - jC''(\omega)$$

$$Z(\omega) = Z'(\omega) - jZ''(\omega)$$

$$C''(\omega) = \frac{Z'(\omega)}{\omega |Z(\omega)|^2}$$

The relaxation time constant, τ_0, was calculated by using the following equation:

$$\tau_0 = \frac{1}{2\pi f_0}$$

where f_0 is the frequency at the maximum imaginary capacitance (C'').

Total static capacitance (C_0) was estimated from a $C''(\omega)$ over frequency plot. The integrated area (A) of the $C''(\omega)$ from f_{max} to f_{min} is related to the C_0 of the porous carbons based on the following equation based on the Kronig-Kramers relations:

$$A = -\int_{-\infty}^{\infty} C''(\omega) d \log f = 0.682 C_0$$

As it is highly challenging to obtain an EIS plot at a very low frequency, the equation was modified to deduce the C_0 value at high frequencies from f_0 to 10^5 as below:[23]

$$C_0 = -\frac{2}{0.682} \int_{f_0}^{10^5} C''(\omega) d \log f$$

Results and discussion

A 1D-HCNB-x was successfully synthesized as shown in Fig. 1a. In a typical synthesis, CoFe-PBA particles with a highly uniform size of 1 μm were first homogeneously dispersed in polyacrylonitrile solution (Fig. 1b). The dispersion of CoFe-PBA particles in PAN was then electrospun to obtain 1D-CoFe-PBA (Fig. 1c). The FESEM image of the as-prepared 1D-CoFe-PBA demonstrates a necklace-like nanoarchitecture (Fig. 1d). It was then subjected to carbonization at 800 °C to obtain 1D-CoFe-PBA/C. From the TEM image, the CoFe-PBA particles disintegrate within the carbon shell derived from PAN, hence creating hollow cavities *via* the Kirkendall effect (Fig. 1e).[24–26] Within the hollow cavities, there are numerous metal nanoparticles formed by thermal crystallization as the atomic shift occurs actively during carbonization (Fig. 1f). Upon acid washing, the metal nanoparticles were successfully removed, and a 1D-HCNB-x was obtained after the second carbonization. The TEM images of 1D-HCNB-900 show obvious hollowness without a trace of metal nanoparticles in the necklace-like nanoarchitecture (Fig. 1g and h).

The XRD spectrum of 1D-CoFe-PBA/C shows clear peaks corresponding to Co/Fe nanoparticles (Fig. 2a).[27] In contrast, the XRD spectrum of 1D-HCNB-900 demonstrates two broad peaks at about 26° and 45° without other notable peaks corresponding to Co/Fe nanoparticles (Fig. 2a). The XRD peaks at 26° and 45° are assigned to the (002) and (101) lattice planes of graphitic carbon.[11,22] The broad peaks at around 26° and 45°, therefore, indicate that 1D-HCNB-900 is an amorphous carbon. The HRTEM image of 1D-CoFe-PBA/C shows the amorphous carbon matrix embedding a dense Co/Fe nanoparticle. Due to the thermal catalytic effect of Co and Fe, numerous graphitic carbon layers are formed around the Co/Fe nanoparticles (Fig. 2b).[28] In contrast, Co/Fe nanoparticles are successfully removed in 1D-HCNB-900, while leaving graphitic carbon layers in the amorphous carbon matrix (Fig. 1g and 2a,c).

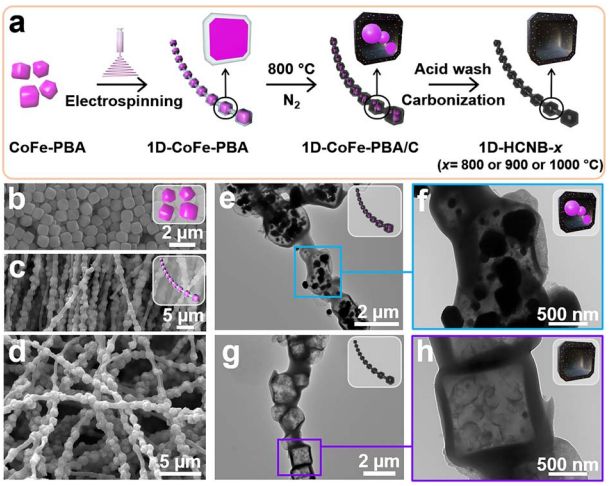

Fig. 1 (a) Schematic description of the synthesis of 1D-HCNB-x. FESEM images of (b) CoFe-PBA, (c) 1D-CoFe-PBA, and (d) 1D-CoFe-PBA/C. TEM images of (e, f) 1D-CoFe-PBA/C and (g, h) 1D-HCNB-900.

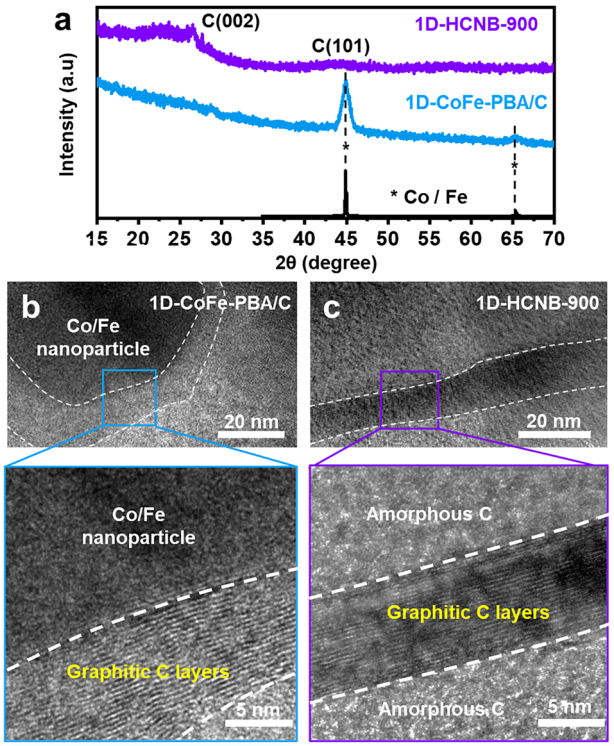

Fig. 2 (a) XRD spectra of 1D-CoFe-PBA/C and 1D-HCNB-900. HRTEM images of (b) 1D-CoFe-PBA/C and (c) 1D-HCNB-900.

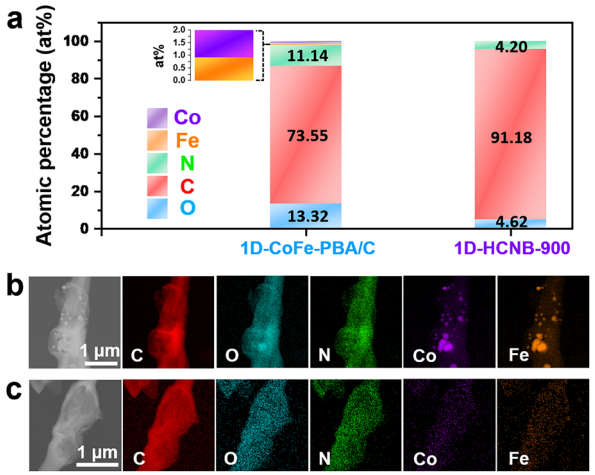

Fig. 3 (a) Atomic percentage of 1D-CoFe-PBA/C and 1D-HCNB-900 derived from their survey XPS spectra. Dark-field STEM image and corresponding elemental mapping images of (b) 1D-CoFe-PBA/C and (c) 1D-HCNB-900.

To further investigate the surface chemistry and elemental compositions, XPS was conducted. From the survey XPS spectra, carbon (C), nitrogen (N), and oxygen (O) atoms are identified in both 1D-CoFe-PBA/C and 1D-HCNB-900 (Fig. S1a and Table S1†). The content of each atom, however, varies significantly between the two samples. Typically, the surface of 1D-CoFe-PBA/C is more enriched with N and O atoms than that of 1D-HCNB-900 (Fig. 3a). Such a decrease in the N and O contents of 1D-HCNB-900 is mainly caused during the second carbonization at 900 °C. At such a high temperature, both N and O atoms tend to get released as gas molecules, while the C atoms undergo a rearrangement to extend the carbon matrix. This, in turn, results in a relative increase in the content of C atoms in 1D-HCNB-900 to as high as 91.18 at% (Fig. 3a and Table S1†). The high-resolution XPS (HRXPS) spectra for C 1s and N 1s of the two samples demonstrate that they possess an N-doped carbon matrix (Fig. S1b and c†).

Also, the HRXPS spectra of C 1s reveal that the carbon matrix of 1D-CoFe-PBA/C is more oxidized as compared to that of 1D-HCNB-900 (Fig. S1b†). While the peaks for the three non-metal elements (C, N, and O) are present in both samples, the peaks for Co and Fe are only detected from 1D-CoFe-PBA/C (Fig. S1a†). This is further confirmed by the HRXPS spectra for Co 2p and Fe 2p of 1D-CoFe-PBA/C showing obvious peaks whereas those of 1D-HCNB-900 only show background noise without any distinct peak (Fig. S2†). Based on the survey XPS spectrum, 1D-CoFe-PBA/C involves 0.91 at% of Fe and 1.08 at% of Co (Fig. 3a and Table S1†). The elemental mappings of 1D-CoFe-PBA/C demonstrate that C, N, and O atoms are uniformly distributed across the structure, along with dense nanoparticles of Co and Fe (Fig. 3b and S3†). 1D-HCNB-900, on the other hand, shows uniform distribution of all elements (C, N, O, Co and Fe) without a trace of metallic nanoparticles (Fig. 3c and S4†). Based on XRD, HRTEM, XPS, and elemental mapping analyses, we expect that Co and Fe in 1D-HCNB-900 mainly exist as ultra-small nanoclusters in the necklace-like porous carbon.

For the supercapacitor study, 1D-HCNB-x were prepared at different carbonization temperatures (800, 900, and 1000 °C) to optimize the carbonization condition. It is generally known that carbonization temperatures exert a significant influence on the porosity and the specific surface area of carbon materials.[29,30] N_2 adsorption/desorption isotherms of the three 1D-HCNB-x carbonized at different temperatures were, therefore, obtained to understand their porosity and specific surface area. Their isotherm curves demonstrate a large initial nitrogen uptake at $P/P_0 < 0.1$, indicating that they are highly microporous carbons (Fig. 4a).[11,29] Typically, 1D-HCNB-900 has the highest initial nitrogen uptake in micropores, followed by 1D-HCNB-1000 and then 1D-HCNB-800. This leads to 1D-HCNB-900 having the largest specific surface area (S_{BET}) of 457.6 $m^2\ g^{-1}$ among the samples (Table S2†). The lower S_{BET} value of 1D-HCNB-1000 as compared to that of 1D-HCNB-900 is potentially due to the collapse of porous structures or the merging of small nanopores to form larger nanopores at such a high carbonization temperature of 1000 °C.[29] The isotherm curves of all carbon samples have upward tailing at high P/P_0 of above 0.9 due to the presence of abundant hollow cavities (Fig. 4a).[11,31] The pattern of the isotherms, therefore, corresponds well with the unique nanoarchitecture of 1D-HCNB-x. Their NLDFT pore size distribution curves agree with the isotherm data that 1D-HCNB-900 has the greatest micropore volume among the samples, therefore, contributing to its large S_{BET} (Fig. 4b).

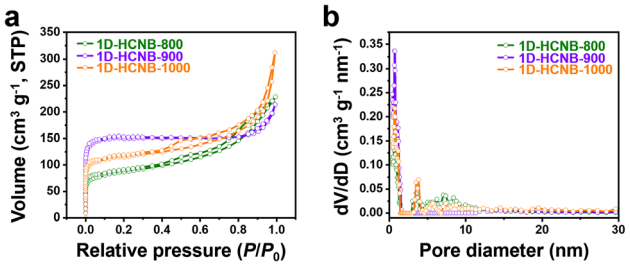

Fig. 4 (a) Nitrogen adsorption/desorption isotherms and (b) NLDFT pore size distribution curves of 1D-HCNB-800, 1D-HCNB-900, and 1D-HCNB-1000.

Based on the detailed characterization studies, the 1D-HCNB-*x* present several advantages that potentially lead to high performance in supercapacitors. The most notable advantage is their unique nanoarchitecture hybridizing two dimensionalities of 1D and 0D. Typically, 1D materials offer efficient axial electron transport to improve the conductivity of materials.[13] The 0D nanoboxes of the 1D-HCNB-*x* present hollow structures that are known to facilitate shorter diffusion pathways by serving as reservoirs for electrolyte ions, therefore contributing to the rate capability in energy-storage applications (Fig. 5a).[11,12] As such, we evaluated the supercapacitor performance of the 1D-HCNB-*x* in a three-electrode system. The CV curves of 1D-CoFe-PBA/C and three types of 1D-HCNB-*x* demonstrate a quasi-rectangular shape, especially at high scan rates, indicating that their energy-storing mechanism is mainly EDLC (Fig. S5†). Although the quasi-rectangular shape of the CV curve is relatively well-maintained even at a high scan rate of 500 mV s^{-1}, there are clear differences in the amount of charge being stored and released among the samples (Fig. S5†). To further investigate the difference in the charge–discharge behavior between the samples, GCD curves were also measured (Fig. S6†). At a low current density of 2 A g^{-1}, the specific capacitance of 370.0, 332.2, 153.4, and 66.6 F g^{-1} is obtained by 1D-HCNB-900, 1D-HCNB-800, 1D-HCNB-1000, and 1D-CoFe-PBA/C, respectively (Fig. 5b and Table S3†). As compared to 1D-CoFe-PBA/C, all 1D-HCNB-*x* have greatly improved specific capacitances by at least twice to more than five times (Fig. S6 and Tables S3, S4†). Such great improvements in specific capacitance are achieved mainly due to the two following reasons: (1) The removal of dense and heavy metallic nanoparticles in the carbon matrix contributes to a greater amount of charge being stored per given mass of the sample. (2) Nanoclusters of Fe and Co increase the faradaic usage of metal atoms in the 1D-HCNB-*x* during charge–discharge processes, thus generating pseudocapacitance more efficiently. Among the 1D-HCNB-*x*, 1D-HCNB-900 exhibits the highest specific capacitance mainly because it has the highest specific surface area, and its specific capacitance is superior to those in previous studies (Fig. 4a and Tables S2, S5†).

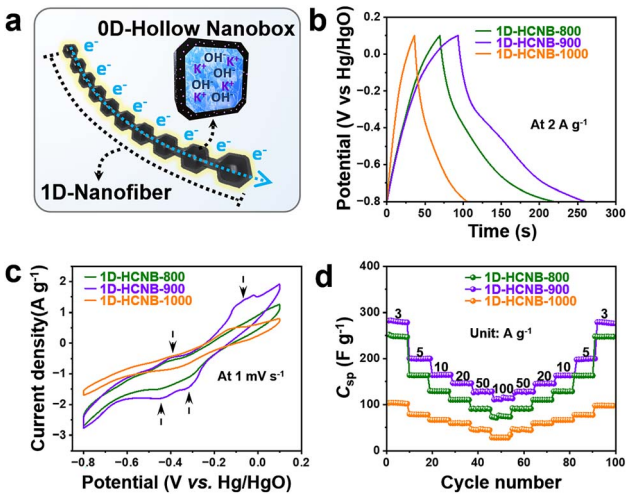

Fig. 5 (a) Schematic showing the advantage of 1D-HCNB-*x* as the electrode material for supercapacitors. (b) GCD curves at 2 A g^{-1}, (c) CV curves at 1 mV s^{-1}, and (d) rate capabilities over a range of current densities (3 to 100 A g^{-1}). All supercapacitor measurements were conducted in 2 M KOH.

Despite 1D-HCNB-1000 having a higher specific surface area than 1D-HCNB-800, it has a much lower specific capacitance potentially due to its nanopores being collapsed and closed at the high carbonization temperature of 1000 °C, leaving a significant portion of its surface area electrochemically inaccessible/inactive to form an electrochemical double layer. In addition, the XRD pattern of 1D-HCNB-1000 indicates the presence of Co/Fe nanoparticles in the carbon matrix (Fig. S7a†), and both Co and Fe peaks are detected by XPS analysis of 1D-HCNB-1000 (Fig. S7b–d†). This indicates that both Co and Fe atoms tend to aggregate and crystallize to form their respective nanoparticles at a very high carbonization temperature of 1000 °C. The formation of Co/Fe nanoparticles, therefore, leads to a significantly limited pseudocapacitance being generated on the surface of nanoparticles while leaving the unexposed dense metallic core electrochemically redundant. From the CV curves of the 1D-HCNB-*x* at a low scan rate of 1 mV s^{-1}, several redox peaks attributable to the doped heteroatoms (N, Co and Fe) become more notable, therefore storing additional charge in the form of pseudocapacitance (Fig. 5c). In contrast, the CV curve of 1D-CoFe-PBA/C at 1 mV s^{-1} does not exhibit such a redox peak, thus indicating the importance of doping the carbon matrix with highly dispersed metal nanoclusters to maximize the involvement of each metal atom to serve as a redox active site (Fig. S8†). It can be observed that the corresponding redox peaks of 1D-HCNB-1000 are also highly attenuated due to the same reason (Fig. 5c). As the appearance of pseudocapacitance is more conspicuous at low scan rates and current densities in the CV and the GCD curves, respectively, it is necessary to investigate the rate capabilities of the three carbon samples. From the specific capacitance at various current densities from 3 to 100 A g^{-1}, the rate capabilities of 29.7, 39.4, and 57.2% are achieved by 1D-HCNB-800, 1D-HCNB-900, and 1D-HCNB-1000, respectively (Fig. 5d and S9a†). It is noteworthy that 1D-HCNB-1000 has the greatest rate capability potentially because it has the lowest portion of electrochemically accessible/active surface area among the samples due to the closed nanopores and the dense metallic nanoparticles. All

1D-HCNB-x exhibit great restoration of specific capacitance at the subsequent current densities in the reverse order from 100 to 3 A g^{-1}, indicating their great rate tolerance at rapidly varied current densities (Fig. 5d).

To further evaluate the electrochemical behavior of 1D-CoFe-PBA/C and 1D-HCNB-x, EIS analysis was conducted. In each of the Nyquist plots of the 1D-HCNB-x, there is no obvious appearance of a semi-circle in the high frequency region because they present EDLC-dominant energy storing behavior. The nearly vertical slope of the Nyquist plots in the low frequency region further confirms their capacitive behavior (Fig. 6a).[32] In contrast, the Nyquist plot of 1D-CoFe-PBA/C demonstrates a rather gradual slope in the low frequency region, and a weak trace of a semi-circle in the high frequency region due to the presence of Co/Fe nanoparticles (Fig. S9b†). The Z' axis intercept point of the Nyquist plot represents the equivalent series resistance (ESR) which is comprised of various resistive factors, including the intrinsic resistance of the material, contact resistance, and solution resistance.[33,34] As the samples were tested under the same electrochemical system, the trend of the ESR value is, therefore, strongly associated with the intrinsic resistance of the material. Based on the Nyquist plots, both 1D-HCNB-900 and 1D-HCNB-1000 have similar ESR values of 0.8 Ω, while 1D-HCNB-800 has an ESR value of 1.4 Ω (Fig. 6a). This indicates that the 1D-HCNB-x obtained at higher carbonization temperatures tend to have lower intrinsic resistance. The ESR value of 1D-CoFe-PBA/C (1.2 Ω) is slightly lower than that of 1D-HCNB-800 (1.4 Ω) potentially due to its abundant metal nanoparticles contributing to the electrical conductivity.[35] As a part of the EIS analysis, the relaxation time constant (τ_0) was calculated using the frequency at which the highest imaginary capacitance is achieved (Fig. 6b). Typically, τ_0 reflects the rate capability of the porous electrode. As the carbonization temperature for 1D-HCNB-x increases from 800 to 900 to 1000 °C, the τ_0 value decreases from 0.20 s to 0.12 s to 0.06 s, hence indicating that the rate capability of 1D-HCNB-x increases at higher carbonization temperatures (Fig. 6c). Such a trend largely corresponds to the capacitance retention rate calculated from the ratio of specific capacitance at 100 A g^{-1} to that at 2 A g^{-1} (Fig. 6c). Based on the total static capacitance (C_0) calculated from EIS, the level of electrochemically wettable surface area in a static state can be deduced. Among the samples, 1D-HCNB-800 and 1D-HCNB-900 demonstrate higher C_0 values of 75.6 and 87.2 F g^{-1}, respectively, as compared to 1D-HCNB-1000 (42.4 F g^{-1}) (Fig. S10†). This indicates that the successful removal of Co/Fe nanoparticles in the porous carbon matrix is essential to maximize the electrochemically wettable surface area.

As 1D-HCNB-900 is found to be an optimized electrode material for a supercapacitor, it was further evaluated for its long-term cyclability. In the cyclability test, the GCD curves at 10 A g^{-1} were measured 15 000 times, and the values of specific capacitance were calculated. Fig. 6c shows that 1D-HCNB-900 does not experience an apparent decay in capacitance, indicating that it is highly stable over repeated charge–discharge processes without losing specific capacitance. In contrast, 1D-CoFe-PBA/C experiences significant capacitance decay even during the first 1000 cycles, and the loss of capacitance reaches 67.6% after 12 000 cycles (Fig. S11†). Such a great loss of capacitance is potentially due to an inevitable evolution of hydrogen and oxygen gas molecules by Co/Fe nanoparticles, causing the gradual loss of 1D-CoFe-PBA/C from the current collector (Fig. S8†). The coulombic efficiency of 1D-HCNB-900 was also investigated to see how efficiently it can handle the stored charge. It turns out that its coulombic efficiency is stable over 15 000 cycles, although the value is above 100% (Fig. 6d). It is attributable to the additional cathodic current generated from potential side reactions such as reduction of dissolved metal ions and oxygen molecules. The presence of large metal nanoparticles due to the reduction of metal ions is observed from the TEM image of 1D-HCNB-900 after stability testing (Fig. S12†).

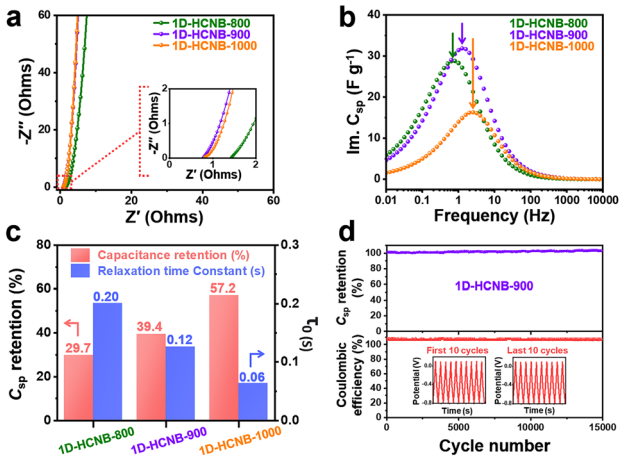

Fig. 6 (a) Nyquist plots (inset shows the high frequency region) of 1D-HCNB-800, 1D-HCNB-900, and 1D-HCNB-1000. (b) Imaginary part of the complex capacitance of 1D-HCNB-x across the frequency range (10 mHz to 100 kHz). (c) Specific capacitance retention rate (2 A g^{-1} to 100 A g^{-1}) and relaxation time constant (τ_0) of 1D-HCNB-x. (d) Percentage of capacitance retention and coulombic efficiency of 1D-HCNB-900 over 15 000 cycles at 10 A g^{-1}. All supercapacitor measurements were conducted in 2 M KOH.

Conclusions

In this study, we successfully demonstrate the synthesis of a novel necklace-like Co, Fe and N co-doped 1D-assembly of hollow carbon nanoboxes and its potential for supercapacitor application. The necklace-like morphology of PAN embedding CoFe-PBA particles (1D-CoFe-PBA) is obtained by electrospinning. Direct carbonization of 1D-CoFe-PBA, in turn, results in 1D-CoFe-PBA/C which involves numerous metal nanoparticles in the carbon matrix. As the presence of large metal nanoparticles adversely influences the specific capacitance by increasing the density of the electrode materials, the metal nanoparticles were removed by acid washing prior to a second carbonization. The resulting material exhibits a unique 1D-assembly of hollow carbon nanoboxes, which is a highly desirable nanoarchitecture toward supercapacitor application. With

the help of its hybrid nanoarchitecture of 0D and 1D features, the 1D-HCNB-*x* contain reservoirs for electrolyte ions to improve rate capability and high axial electron conductivity, respectively. The presence of Fe and Co dopants in the carbon matrix also contributes to pseudocapacitive charge storage to further improve specific capacitance. The optimized sample of 1D-HCNB-900, therefore, generates a specific capacitance of 370.0 F g^{-1} at a current density of 2 A g^{-1}, high rate capability and tolerance, and great cyclability without any capacitance decay over 15 000 consecutive charge–discharge cycles.

Author contributions

M. K. and C. W. conducted the experiments. M. K. wrote the manuscript. M. K., C. W., J. E., and A. A. characterized the materials. J. E., T. P., N. A., J. N., M. H., and A. E. R revised the manuscript. J. W. L and Y. Y. performed conceptualization.

Conflicts of interest

There are no conflicts to declare.

Acknowledgements

This research was supported by the Principal Research Program (PNK8740) at the Korea Institute of Materials Science (KIMS).

References

1 Z. Zhang, T. Ding, Q. Zhou, Y. Sun, M. Qu, Z. Zeng, Y. Ju, L. Li, K. Wang and F. Chi, *Renewable Sustainable Energy Rev.*, 2021, **148**, 111263.
2 A. G. Olabi, C. Onumaegbu, T. Wilberforce, M. Ramadan, M. A. Abdelkareem and A. H. Al-Alami, *Energy*, 2021, **214**, 118987.
3 H. Qutaish, S. A. Han, Y. Rehman, K. Konstantinov, M.-S. Park and J. Ho Kim, *Sci. Technol. Adv. Mater.*, 2022, **23**, 169–188.
4 Y. Li, J. Zhang, Q. Chen, X. Xia and M. Chen, *Adv. Mater.*, 2021, **33**, 2100855.
5 H. Chen, T. N. Cong, W. Yang, C. Tan, Y. Li and Y. Ding, *Prog. Nat. Sci.*, 2009, **19**, 291–312.
6 M. Kim, H. Lim, C. Wang, K. Kani, G. Kwon, J. You, H. Park, A. A. Alshehri, Y. G. Alghamidi, K. A. Alzahrani, J. Na, J. Li, Y. Yamauchi and J. Kim, *Mater. Lett.*, 2019, **253**, 178–182.
7 R. R. Salunkhe, Y. V. Kaneti, J. Kim, J. H. Kim and Y. Yamauchi, *Acc. Chem. Res.*, 2016, **49**, 2796–2806.
8 M. Kim, R. Xin, J. Earnshaw, J. Tang, J. P. Hill, A. Ashok, A. K. Nanjundan, J. Kim, C. Young, Y. Sugahara, J. Na and Y. Yamauchi, *Nat. Protoc.*, 2022, DOI: **10.1038/s41596-022-00718-2**.
9 M. Kim, K. L. Firestein, J. F. S. Fernando, X. Xu, H. Lim, D. V. Golberg, J. Na, J. Kim, H. Nara, J. Tang and Y. Yamauchi, *Chem. Sci.*, 2022, **13**, 10836–10845.
10 Y. Hyeon, J. Lee, H. Qutaish, S. A. Han, S. H. Choi, S. W. Moon, M.-S. Park, D. Whang and J. H. Kim, *Energy Storage Mater.*, 2020, **33**, 95–107.
11 M. Kim, X. Xu, R. Xin, J. Earnshaw, A. Ashok, J. Kim, T. Park, A. K. Nanjundan, W. A. El-Said, J. W. Yi, J. Na and Y. Yamauchi, *ACS Appl. Mater. Interfaces*, 2021, **13**, 52034–52043.
12 M. Kim, J. F. S. Fernando, J. Wang, A. K. Nanjundan, J. Na, M. S. A. Hossain, H. Nara, D. Martin, Y. Sugahara, D. Golberg and Y. Yamauchi, *Chem. Commun.*, 2022, **58**, 863–866.
13 D. P. Chatterjee and A. K. Nandi, *J. Mater. Chem. A*, 2021, **9**, 15880–15918.
14 S. Kumar, G. Saeed, L. Zhu, K. N. Hui, N. H. Kim and J. H. Lee, *Chem. Eng. J.*, 2021, **403**, 126352.
15 M. Hu, J. Reboul, S. Furukawa, N. L. Torad, Q. Ji, P. Srinivasu, K. Ariga, S. Kitagawa and Y. Yamauchi, *J. Am. Chem. Soc.*, 2012, **134**, 2864–2867.
16 A. M. Boies, C. Hoecker, A. Bhalerao, N. Kateris, J. de La Verpilliere, B. Graves and F. Smail, *Small*, 2019, **15**, 1900520.
17 S. Maji, R. G. Shrestha, J. Lee, S. A. Han, J. P. Hill, J. H. Kim, K. Ariga and L. K. Shrestha, *Bull. Chem. Soc. Jpn.*, 2021, **94**, 1502–1509.
18 C. Wang, H. Wang, J. Na, Y. Yao, A. Azhar, X. Yan, J. Qi, Y. Yamauchi and J. Li, *Chem. Sci.*, 2021, **12**, 15418–15422.
19 F. Marpaung, T. Park, M. Kim, J. W. Yi, J. Lin, J. Wang, B. Ding, H. Lim, K. Konstantinov, Y. Yamauchi, J. Na and J. Kim, *Nanomaterials*, 2019, **9**, 1796.
20 M. Kim, T. Park, C. Wang, J. Tang, H. Lim, M. S. A. Hossain, M. Konarova, J. W. Yi, J. Na, J. Kim and Y. Yamauchi, *ACS Appl. Mater. Interfaces*, 2020, **12**, 34065–34073.
21 N. L. Torad, M. Hu, S. Ishihara, H. Sukegawa, A. A. Belik, M. Imura, K. Ariga, Y. Sakka and Y. Yamauchi, *Small*, 2014, **10**, 2096–2107.
22 J. Tang, R. R. Salunkhe, J. Liu, N. L. Torad, M. Imura, S. Furukawa and Y. Yamauchi, *J. Am. Chem. Soc.*, 2015, **137**, 1572–1580.
23 S. H. Lee, J. Kim, D. Y. Chung, J. M. Yoo, H. S. Lee, M. J. Kim, B. S. Mun, S. G. Kwon, Y.-E. Sung and T. Hyeon, *J. Am. Chem. Soc.*, 2019, **141**, 2035–2045.
24 C. Wang, J. Kim, M. Kim, H. Lim, M. Zhang, J. You, J.-H. Yun, Y. Bando, J. Li and Y. Yamauchi, *J. Mater. Chem. A*, 2019, **7**, 13743–13750.
25 C. Wang, J. Kim, J. Tang, J. Na, Y.-M. Kang, M. Kim, H. Lim, Y. Bando, J. Li and Y. Yamauchi, *Angew. Chem., Int. Ed.*, 2020, **59**, 2066–2070.
26 M. J. Wang, Z. X. Mao, L. Liu, L. Peng, N. Yang, J. Deng, W. Ding, J. Li and Z. Wei, *Small*, 2018, **14**, 1804183.
27 X. Liang, G. Wang, W. Gu and G. Ji, *Carbon*, 2021, **177**, 97–106.
28 M. Sevilla and A. B. Fuertes, *Carbon*, 2006, **44**, 468–474.
29 C. Young, R. R. Salunkhe, J. Tang, C.-C. Hu, M. Shahabuddin, E. Yanmaz, M. S. A. Hossain, J. H. Kim and Y. Yamauchi, *Phys. Chem. Chem. Phys.*, 2016, **18**, 29308–29315.
30 R. Chatterjee, B. Sajjadi, W.-Y. Chen, D. L. Mattern, N. Hammer, V. Raman and A. Dorris, *Front. Energy Res.*, 2020, **8**, 85.
31 G. Li, X. Yan, P. Mei, Y. Jiang, Y. Zhang, F. Deng, Y. Xiong and H. Tang, *J. Mater. Sci.: Mater. Electron.*, 2018, **29**, 7718–7724.

32 Z. Niu, W. Zhou, J. Chen, G. Feng, H. Li, W. Ma, J. Li, H. Dong, Y. Ren, D. Zhao and S. Xie, *Energy Environ. Sci.*, 2011, **4**, 1440–1446.
33 R. Zhang, X. Jing, Y. Chu, L. Wang, W. Kang, D. Wei, H. Li and S. Xiong, *J. Mater. Chem. A*, 2018, **6**, 17730–17739.
34 S. Jia, Y. Wang, G. Xin, S. Zhou, P. Tian and J. Zang, *Electrochim. Acta*, 2016, **196**, 527–534.
35 Y. Wang, S. Lu, W. He, S. Gong, Y. Zhang, X. Zhao, Y. Fu and Z. Zhu, *Sci. Rep.*, 2022, **12**, 10448.